

# Spatial and molecular profiling of classic Hodgkin lymphoma reveals an immunosuppressive mononuclear phagocyte network

**Benjamin Stewart**

University of Cambridge

**Martin Fergie**

University of Manchester

**Matthew Young**

Wellcome Trust Sanger Institute <https://orcid.org/0000-0003-0937-5290>

**Claire Jones**

Newcastle upon Tyne NHS Foundation Trust

**Ashwin Sachdeva**

University of Manchester

**Alex Blain**

Newcastle University

**Chris Bacon**

Newcastle University

**Vikki Rand**

Teeside University

**John Ferdinand**

University of Cambridge

**Kylie James**

Garvan Institute of Medical Research

**Krishnaa Mahbubani**

University of Cambridge

**Liz Hook**

University of Cambridge

**Nicolaas Jonas**

University of Cambridge

**Nicholas Coleman**

University of Cambridge

**Kourosh Saeb-Parsy**

Cambridge University <https://orcid.org/0000-0002-0633-3696>

**Matthew Collin**

University of Newcastle <https://orcid.org/0000-0001-6585-9586>

**Menna Clatworthy**

University of Cambridge

**Sam Behjati**

Wellcome Sanger Institute <https://orcid.org/0000-0002-6600-7665>

**Christopher Carey** (✉ [christopher.carey@newcastle.ac.uk](mailto:christopher.carey@newcastle.ac.uk))

Newcastle University <https://orcid.org/0000-0002-4293-3920>

---

**Brief Communication**

**Keywords:** Lymphoid neoplasia, Hodgkin lymphoma, Hodgkin's disease, Classic Hodgkin lymphoma, tumor microenvironment, microenvironment, dendritic cells, mononuclear phagocytes, classical monocytes, macrophages, Hodgkin cells, immunobiology, immunotherapy, Transcriptomics, proteomics

**Posted Date:** March 14th, 2022

**DOI:** <https://doi.org/10.21203/rs.3.rs-1233380/v2>

**License:**   This work is licensed under a Creative Commons Attribution 4.0 International License.

[Read Full License](#)

---

# Abstract

Although a lymph node infiltrated by classic Hodgkin lymphoma (cHL) is mostly composed of nonneoplastic immune cells, the malignant Hodgkin Reed-Sternberg cells (HRSC) successfully suppress an anti-tumor immune response, creating a cancer-permissive microenvironment. Accordingly, unleashing the dormant immune cells, for example by checkpoint inhibition, has been a central focus of recent therapeutic advances for this disease. Despite the efficacy of PD-1 blockade in relapsed cHL, a significant proportion of patients have suboptimal or non-durable responses, which may reflect HRSC and microenvironmental adaptation.

Here, we profiled the global immune cell composition of normal and diseased lymph nodes by singlecell RNA sequencing, as a basis for interrogating the immediate vicinity of HRSC. We did so regionally and at cellular resolution, using spatial transcriptomics and multiplexed immunofluorescence, on fixed cHL tissue sections. It is established that tumor associated macrophages (TAMs) are associated with inferior outcomes following combination chemotherapy, but the function, interactions, and distribution of TAMs, and other mononuclear phagocytes, have not been fully explored.

Our analyses revealed specific immune cells and functional states associated with HRSC. We discovered a non-random spatial organization of immunoregulatory mononuclear phagocytes (TAMs and classical monocytes) around HRSC, which express the immune checkpoints PD-L1, TIM-3, and the tryptophan-catabolizing protein IDO1. Dendritic cells (DC), key antigen presenting cells, are regionally polarized according to subtype. Specific DCs are spatially associated with the HRSC 'neighborhood' (cDC2), but plasmacytoid DCs and 'activated' DCs are excluded. These findings provide a basis for rational targeting and activation of the anti-tumor immune response in cHL.

## Key Points

- Mononuclear phagocytes are signaling hubs around malignant Reed-Sternberg cells in Classic Hodgkin lymphoma, potentiating immunosuppression.
- Dendritic cells are spatially polarized, with cDC2 closely associated with malignant cells, and plasmacytoid DCs and activated DCs excluded.

## Introduction

Classic Hodgkin lymphoma (cHL) accounts for 12-15% of lymphoma diagnoses and occurs most frequently in adolescents and young adults, with another peak of incidence in older adults. Multi-agent cytotoxic chemotherapy (including selective use of radiotherapy) is curative in 80-95% of patients; in adults the potential for cure is largely determined by the disease stage<sup>1-3</sup>. However, for patients with

relapsed or refractory disease, the prospect of cure or long-term disease control is significantly diminished.

A cHL tumor is characterized by a minority population of neoplastic CD30<sup>+</sup> Hodgkin Reed-Sternberg Cells (HRSC), comprising 1-5% of cells, derived from germinal center (GC) B cells<sup>4</sup>. HRSC survive within a tumor microenvironment (TME), primarily composed of immune cells, containing abundant T-cells and a network of mononuclear phagocytes (MNP), including macrophages, monocytes, and dendritic cells (DC)<sup>4</sup>.

HRSC establish an immunosuppressive niche through multiple mechanisms, including downregulation of major histocompatibility complex (MHC) proteins, and enhanced expression of programmed cell death ligand-1 (PD-L1), resulting from 9p23-p24 copy number gain or amplification<sup>5,6</sup>. PD-L1 diminishes T-cell activation by ligation of its cognate receptor PD-1, which has been targeted by anti-PD-1 immune checkpoint blockade in relapsed/refractory disease, with evidence of therapeutic efficacy in the majority of patients<sup>7-9</sup>. Indeed, PD-L1 expression by HRSC and immune cells, including CD68<sup>+</sup> tumor-associated macrophages (TAM), is almost universal in cHL<sup>10</sup>. However, the phenotypes, roles, and intercellular communication networks of MNP within the TME remain largely unknown. We hypothesize that MNPs extend and maintain the immunosuppressive niche through multiple mechanisms. Here, we present a robust characterization of the critical intercellular communication networks in the tumor microenvironment, with the aim of identifying novel therapeutic targets.

## Methods

### *Single cell transcriptional analysis*

To gain an overview of the cellular ecosystem of cHL, we compiled a census of 243,753 single cell transcriptomes, from lymphoma affected and unaffected lymph nodes. We sourced data from Aoki *et al*<sup>11</sup> incorporating droplet encapsulation single cell transcriptomes (10X genomics platform) from reactive and cHL nodes (Fig. 1a). Additionally, we performed scRNAseq (10X genomics platform) with cell suspensions from healthy lymph nodes acquired from deceased organ donors, and two lymphoma lymph nodes, one with nodular sclerosis cHL (NSCHL), and one with nodular lymphocyte predominant Hodgkin lymphoma (NLPHL), a biologically distinct subtype of Hodgkin lymphoma (Fig. 1a). Together, the combined dataset comprises tissue from 13 non-lymphoma affected donors (8 deceased donors and 5 donors with reactive lymph node hyperplasia), plus one NLPHL and 23 cHL lymph nodes (Fig. 1a). After quality control (Supplementary Methods, Supplementary Fig. 1a-b), we performed dataset integration and dimensionality reduction using single-cell variational inference<sup>12</sup> and annotated cell types on the basis of marker genes and external dataset validation (Fig. 1b, Supplementary Fig. 1c-e).

### *Tissue samples for scRNAseq*

Healthy lymph nodes, unaffected by neoplastic disease, were acquired from donation after circulatory death (DCD) adult donors at the time of removal of organs for transplantation by the Cambridge Biorepository for Translational Medicine (CBTM) with ethical approval (reference 15/EE/0152, East of England—Cambridge South Research Ethics Committee) and consent from donor families. Lymph node samples were collected from inguinal, mesenteric, and thoracic regions at the end of the organ donation procedure, within 1-2 hours of cessation of circulation under cold ischaemic conditions. Lymph node specimens were maintained in ice-cold 0.9% saline for transport. Tissue was dissociated and processed as previously described<sup>13</sup>. Lymph node data from (290b, 298c, 302c) are shared with James *et al.* and were processed with additional flow sorting as described<sup>13</sup>. Patients who donated diseased tissue for scRNAseq were enrolled in the 'Investigating how childhood tumors and congenital disease develop' study (NHS National Research Ethics Service reference 16/EE/0394).

### *Single cell RNA sequencing analysis*

Single-cell RNA sequencing data from Hodgkin lymphoma specimens were acquired by direct data transfer from the Stiedl lab (University of British Columbia) as a raw counts matrix<sup>11</sup>. Mapping and quantification of scRNAseq generated for this study (Wellcome Sanger Institute dataset) was performed using the kallisto-bustools toolkit (0.24.4)<sup>14</sup>, against the GRCh38 human reference. The unfiltered count matrix was profiled using the *defaultDrops* function in the DropletUtils package (1.10.3)<sup>15</sup>, in R (4.0.4).

We performed data integration with batch correction (using donor as the batch key) and dimensionality reduction concurrently by training a single-cell variational inference model using the scvi-tools python package (version 0.9.0a0)<sup>12</sup>. We completed quality control on the integrated dataset (Supplementary methods, Supplementary Fig. 1a-b). A 15-dimensional latent representation was used as input to nearest neighbor graph construction, Uniform Manifold and Approximation (UMAP), and Leiden clustering in scanpy. Marker genes were calculated using the tf-idf metric and genes were ranked by the tf-idf metric, and p values calculated by a hypergeometric test, corrected for multiple testing (Benjamini-Hochberg method)<sup>16</sup>. These marker genes were used as a guide to manual annotation of cell types. Cell types were annotated according to canonical marker expression (Supplementary Fig. 1c), supplemented with labeling using the celltypist python package (0.1.15)<sup>17</sup>. Concordance between annotated celltype labels and predicted reference annotations was assessed by calculating the Jaccard distance between cell label strings (Supplementary Fig. 1d-e). Cell type predictions between the King *et al.* B cell atlas<sup>18</sup> was

calculated by training a multilayer perceptron classifier on the reference data and calculating predictions on unseen test data, implemented in the scikit learn package (0.24.2)<sup>19</sup>.

Relative abundance analysis was performed using the MiloR package (0.99.1)<sup>20</sup>. The annotated dataset was represented as a k=30 nearest neighbor graph calculated in scVI latent space. This graph representation was partitioned into 22,573 overlapping neighborhoods, and cell counts per 10X channel were calculated per neighborhood. Differential abundance between disease and health was calculated using the *testNhoods* function, setting the design as ~center + disease, and norm.method="TMM".

Ligand receptor analysis was performed using CellPhoneDB (version 2.1.7)<sup>21</sup>. The count matrix was normalized to 1e4 total counts before input to the python implementation of CellPhoneDB which was run with `-iterations=1000`, `-threshold=0.1`, and `-result-precision=3`.

### *Microarray data analysis*

The GEO accession GSE39133 was downloaded using the GEOquery R package (version 2.60.0)<sup>22</sup>. We performed differential expression between GC and HRSC samples using limma (version 3.48.1)<sup>23</sup> and derived genesets by retaining genes with an absolute log fold change >3 and adjusted p value <0.01.

### *Transcription factor regulon and network analysis*

Transcription factor regulons data were acquired using the dorothea R package (version 1.3.3)<sup>24</sup>. Regulons with confidence levels "A", "B", and "C" were used to calculate transcription factor activities using the *run\_viper* command.

We derived a network graph of transcription factors and targets using data from the OmnipathR R package (version 3.12)<sup>25</sup>, plotting edges between transcription factors and targets, and between targets using the ggraph R package (version 2.0.5).

### *Tissue samples for Nanostring and Multiplexed Immunofluorescence*

The study was approved by a UK NHS Health Research Authority (HRA) Research Tissue Bank (Novopath Biobank, Newcastle upon Tyne Hospitals NHS Foundation Trust, reference number: 17/NE0070). The Research Tissue Bank released link-anonymized, formalin-fixed and paraffin embedded (FFPE) tissue,

from patients with cHL. All tissue samples were surplus to diagnostic requirements and were released in accordance with the terms of the ethical approval.

FFPE tumor biopsies (all excised lymph nodes) were selected from the pathology archives of Newcastle upon Tyne Hospitals NHS Foundation Trust, UK, by members of the Novopath biobank, with appropriate ethical approval (reference: 17/NE0070). Limited, link-anonymized clinical data for study patients were collected by the biobank. Hematoxylin and eosin-stained (H&E) tissue sections and immunohistochemical tissue sections were reviewed by a hematologist, together with the original pathology reports. Fifty-four cases were selected for the study, including biopsies from patients of all ages and histomorphological subtypes (Table 1). Patient biopsies were selected on the basis of high-quality, whole lymph node resection biopsy tissue. Patients with coexisting malignant diagnoses were excluded from the study, even if these were not apparent in the tissue.

### Nanostring spatial transcriptomics

Ten of the FFPE cHL tissue biopsies used in the multiplexed immunofluorescence analysis were selected for *in situ* transcriptomics (Table 1), using the Nanostring GeoMx platform (Nanostring, Seattle, WA). Biopsies were selected based upon year of fixation (2014 onwards), high quality multiplex staining, and successful RNAscope quality control (QC) tests (Advanced Cell Diagnostics, Inc., Newark, CA). Five test slides were prepared, each arrayed with 2 unique, whole tissue biopsy sections; one slide also included reactive lymph node tissue. For each test slide, 4 consecutive 4- $\mu$ m-thick sections were taken from each tissue block, prepared according to the manufacturer's instructions, and numbered 1-4: Slide 1, Hematoxylin & Eosin counterstain; Slide 2, CD45 and PAX5 immunostains (fluorescent IHC); Slide 3, *CD274* (PD-L1) and *PDCD1* (PD-1) - RNAscope probes, DNA counterstain; Slide 4, Oligonucleotide RNA probe hybridization.

Circular regions of interest (ROIs; uniform 300- $\mu$ m diameter) were labeled upon the *CD274/PDCD1* (PD-L1) RNAscope slides, with reference to H&E and IHC slides for histomorphological context. PD-L1 was used to identify HRSC, rather than CD30, as fluorescent labeling with *CD274* probes was more robust in optimization experiments. In all selected tumors, the HRSC-dense areas of tissue were known to be PD-L1+, and HRSC were identified by DAPI signal and nuclear morphology. For each tumor, 3 ROIs were selected in 'PD-L1<sup>high</sup>' areas and 3 ROIs in 'PD-L1<sup>low</sup>' areas of tissue, unless otherwise stated. Assessments of PD-L1 intensity were made by visual inspection of normalized *CD274* probe fluorescent signal within each tumor. Sclerotic bands, germinal centers, and areas of low cellularity were avoided in cHL tissues, by referring to DNA counterstaining and paired IHC. In the control RN tissue, 3 ROIs were labeled in germinal centers and 3 ROIs in interfollicular areas. RNA oligonucleotides from the 'Cancer Transcriptome Atlas' (n = 1812 probes), coupled to photocleavable oligonucleotide tags ('barcodes'), were

hybridized overnight. The following day, hybridized barcodes were released from tissue by UV exposure from each ROI sequentially, before being counted and sequenced on the Illumina HiSeq 2500 platform.

### *Nanostring data analysis*

Quality control steps were performed on exported data to exclude outlier probes and then data were normalized against the 75th percentile of signal from each tumor. Following data QC, 1372 (75.7%) probes were retained for analysis. The nanostring expression matrix (ROI-by-gene) was analyzed by principal component analysis (PCA) using the scanpy python package, before constructing a shared-nearest neighbor graph representation. Briefly, we identified k=10 nearest neighbors in PCA space using the FNN R package, before calculating the Jaccard distance between neighbor vectors after the approach of Levine *et al*<sup>26</sup>. The resulting graph was clustered using the Leiden algorithm<sup>27</sup> with default settings.

Deconvolution was performed by first generating a matrix of one-hot-encodings of marker genes per cell type, including HRSC. We then used the *rlm* function in the MASS R package to perform robust linear regression. The resulting coefficients were treated as fractions to derive counts by multiplying by the number of nuclei in each ROI. These cell count estimates were then used to calculate differential abundance estimates for each cluster using DESeq2<sup>28</sup>. Differential expression analysis between clusters was performed using limma (version 3.48.1)<sup>23</sup>. The top 10 differentially expressed genes per cluster were selected for plotting (Supplementary Fig. 3c)

### *Multiplexed immunofluorescence*

Multiplexed immunofluorescence (IF) was performed by sequentially immunostaining 4- $\mu$ m-thick tissue sections from selected FFPE tumor biopsies, with primary antibodies, secondary reagents, and unique fluorochromes. Each of the two multiplexes comprises 6 primary antibodies, followed by a nuclear counterstain, 4',6-diamidino-2-phenylindole, as per published protocols<sup>10,29,30</sup>. All immunostaining was performed on the automated Ventana Benchmark platform (Roche Diagnostics, Rotkreuz, Switzerland). Slides were then air dried, mounted with Prolong Diamond Anti-fade mounting medium (#P36965; Life Technologies) and stored at 4°C in a light proof box until image acquisition. The target antigens, antibody clones, and dilutions for markers included in this report are listed in Table 2.

### *Image acquisition*

Test regions for multiplex IF analysis were initially identified for each tumor biopsy by reviewing the H&E and immunofluorescence tissue sections at 4x magnification. Three non-overlapping regions of interest were then acquired at 20x magnification for each multiplex panel. Each of these 3 test regions comprised

9 contiguous fields of view (FOVs), arranged as a 3x3 rectangular grid (measuring 2008µm x 1508µm in total). Therefore, there were a total of 27 FOVs per tumor, for each multiplex.

Regions were selected to exclude tissue artifacts, best represent the overall tissue, and to include CD30+ HRSCs. Regions were imaged and deconvoluted using the Vectra multispectral imaging platform (Vectra 3 and Inform 2.4.8, Akoya Biosciences, Marlborough, MA), using specific spectral libraries.

## Results

The cellular ecosystem of cHL encompassed subsets of CD4<sup>+</sup> and CD8<sup>+</sup> T-cells, including regulatory T-cells (Treg), T follicular helper cells (Tfh), and exhausted CD4<sup>+</sup> (ThExh) and CD8<sup>+</sup> T-cells (CD8 TExh) cells (Fig. 1a). ThExh matched the recently identified LAG3<sup>+</sup> subset, and expressed checkpoint molecules and exhaustion markers including *CD27*, *TNFRSF18*, *LAG3*, and *ICOS*<sup>1,31</sup> (Fig. 1b, Supplementary Fig. 1f). The B cell compartment split into two large clusters of memory and naive subsets, in addition to plasmablasts, and germinal center B cells (Fig. 1b, Supplementary Fig. 1c-e).

Within the myeloid compartment, we identified macrophages coexpressing *CD14*, *CD68*, and the M2 polarization markers *FOLR2* and *MRC1* (Fig. 1c-d). These cells were transcriptionally distinct from classical monocytes, which expressed a characteristic signature including *S100A9*, *CD14*, *VCAN*, and *FCN1*<sup>32</sup> (Fig. 1c-d). Amongst DCs, we identified cDC1 (key transcripts: *CLEC9A*, *CADM1*, and *IDO1*) and cDC2 (key transcripts: *CD1C*, *CLEC10A*, and *FCER1A*) (Fig. 1c-d). In addition to cDC1 and cDC2, we also identified a population of *LAMP3*<sup>+</sup> DCs in both healthy and some lymphoma samples, expressing the chemokine receptor *CCR7* and the chemokines *CCL17* and *CCL19*, which we termed “activated DCs” (aDC) consistent with the nomenclature of transcriptionally similar cells described in human thymus and spleen<sup>33,34</sup>, and in murine lung neoplasms<sup>35</sup> (Fig. 1c-d, Supplementary Fig. 1d). We found a population of plasmacytoid DCs (pDC) with a dominant contribution from lymphoma samples (Fig. 1e, Supplementary Fig. 2a), expressing *IL3RA* (CD123), *CLEC4C*, and *CXCR3* (Fig. 1c-d). The undiseased reference samples contributed a rare population of mast cells, expressing characteristic marker genes including *CPA3*, *KIT*, and *TPSAB1* (Fig. 1c-d).

A key challenge in comparing the cellular architecture of lymph nodes lies in quantifying the relative enrichment of different cell-types in health and disease. This has recently been addressed through a differential abundance testing method, based on partially overlapping neighborhoods of cells on a k-NN graph (MiloR tool<sup>20</sup>). Applying MiloR, we represented the integrated manifold as a k-NN graph partitioned into 22,573 overlapping neighborhoods, before statistical testing for differential cell abundance between lymphoma affected and unaffected within each neighborhood (Methods). In lymphoma nodes, the T-cell compartment was polarized towards cytotoxic subsets including NK cells and effector memory CD8<sup>+</sup> T-

cells (CD8 Tem), in addition to CD4<sup>+</sup> T-cells subsets expressing checkpoint apparatus including ThExh and Tfh cells (Fig. 1f, Supplementary Fig. 2b). The association of these subsets with disease subtypes diverged between cHL and NLPHL. Classic HL subtypes were enriched for exhausted T-cell subsets, which contrasted with the NLPHL sample, where the cellular landscape was dominated by cytotoxic subsets (NK cells, CD8 Tem, and CD8 Tcm) (Supplementary Fig. 2c).

To fully appreciate the cHL microenvironment, it is crucial to assess how HRSC influence their immune neighbors. The scRNAseq dataset did not contain a population of HRSC, likely due to the rarity, size, and fragility of these cells. To establish the transcriptional program of HRSC, we leveraged a microarray dataset profiling microdissected HRSC and GCs (Methods)<sup>36</sup>. Differential expression between HRSC and GC established an upregulated HRSC gene signature, including *TNFRSF8* (CD30) (Fig. 1g). Scoring of transcription factor regulons demonstrated activation of NF- $\kappa$ B (*NFKB1* and its activatory heterodimer partner *RELA*) in HRSC (Fig. 1h), consistent with previous reports<sup>37</sup>. We next performed *in silico* identification of molecular interactions between active transcription factors and potential targets within the HRSC geneset (Methods). This demonstrated an NF- $\kappa$ B-centric network coordinating the upregulation of the chemokines *CCL5*, *CCL17*, and *CCL22* capable of the positioning and retention of ThExh via CCR5 and CCR4 ligation (Fig. 1i, Supplementary Fig. 1f).

We used this lymph node-wide account of the immune landscape of Hodgkin lymphoma as a reference to interrogate the cellular composition of cHL tissues. We specified regions surrounding HRSCs, using targeted spatial transcriptomic profiling (Nanostring GeoMx Cancer Transcriptome Atlas), defining 300  $\mu$ m diameter regions of interest (ROI) in both PD-L1<sup>high</sup> and PD-L1<sup>low</sup> regions of 9 NSCHL and 1 Mixed cell cHL (MCCHL) lymph nodes, and follicular and interfollicular regions of one control reactive lymph node (Supplementary Fig. 3a-b). We represented these transcriptional profiles in a shared-nearest neighbor graph and identified 5 types (clusters) of microenvironment across cHL and control lymph nodes (Fig. 2a-b). We deconvoluted the cell composition of each cluster, using our scRNAseq atlas as reference, followed by cell-type count estimation and differential cell-type abundance analysis (Fig. 2c). The five types of microenvironments encompassed two 'neoplastic' HRSC enriched clusters (clusters 3 & 4), two 'non-neoplastic' (i.e. devoid of HRSC signatures; clusters 1 & 5), and one intermediate neighborhood (cluster 2). The two non-neoplastic neighborhoods were PD-L1<sup>low</sup> and represented the normal lymph node follicular microenvironment (cluster 5) or fibrosing regions of diseased lymph nodes (cluster 1). Notably, established fibrotic regions are an adjunct diagnostic histological feature of NSCHL<sup>38</sup>. The neoplastic environments were PD-L1<sup>high</sup> and exhibited divergent leukocyte enrichment. Cluster 3 was enriched for ThExh, Th cells, and NK cells, whereas cluster 4 exhibited myeloid cell infiltration, with enrichment of classical monocytes, macrophages, and cDC2 (Fig. 2c). Differentially expressed genes in cluster 4 suggested potent inflammatory signaling, with high expression of chemokines associated with Th2 responses and CCR3-dependent eosinophil recruitment (*CCL18*, *CCL13*,

*CCL24*, *CCL26*, *CCL23*) and granulocyte attracting chemokines *CXCL1*, and *CXCL6* (Supplementary Fig. 3c). Cluster 1 contained almost exclusively PD-L1<sup>low</sup> regions and was enriched for stromal (fibroblast and endothelial) cells and classical monocytes (Fig. 2c). Differentially expressed genes in this cluster included genes encoding key signaling mediators of fibrosis *FGFR4*, *TGFB2*, and *PTCH1*, in addition to *TNN* encoding the matrix extracellular component tenascin (Supplementary Fig. 3c). Overall, these findings suggest heterogeneous immune infiltrates within the broader cHL microenvironment, some of which may progress to fibrosis.

Given the diversity of MNP enrichment in neoplastic regions, we sought to establish the spatial relationships of MNP subsets within the HRSC niche at single-cell resolution. Using MNP marker gene co-expression patterns in the scRNAseq data (Supplementary Fig. 3d), we designed multiplexed immunofluorescence (IF) panels to identify MNPs in fixed cHL tissue sections. We identified CADM1<sup>+</sup>/CD11c<sup>+</sup> cDC1, CD1c<sup>+</sup>/CD11c<sup>+</sup> cDC2, LAMP3<sup>+</sup> aDC with highly distinctive dendritic morphology, CD123<sup>+</sup> pDC, CD11c<sup>+</sup> monocytes and macrophages (CD11c<sup>+</sup> ONLY), and CD30<sup>+</sup> HRSC (Fig. 2d). We then phenotyped segmented cells and performed neighborhood analyses, taking a 25  $\mu$ m-radius neighborhood around each CD30<sup>+</sup> HRSC and measuring the relative enrichment of MNP subsets in these aggregated neighborhoods, compared to the remaining regions ('non-neighborhood') across the tissue section. This analysis revealed enrichment of cDC2 and CD11c<sup>+</sup> monocytes in the immediate vicinity of HRSC across cHL samples. In contrast, both pDC and aDC were excluded from the HRSC niche and occupy regions with a low density of CD11c<sup>+</sup> cells (Fig. 2e-g, Fig. 3a-h). These findings indicate non-random, active organization of MNP subsets in the immediate HRSC-neighborhood.

We next asked which signals might coordinate the positioning of the MNP subsets and T-cells found in close association with HRSC. To interrogate these ligand-receptor interactions (LRI), we calculated the statistical enrichment of candidate LRI between MNPs and T-cells in our scRNAseq data using the CellPhoneDB tool<sup>21</sup>. This analysis predicted paracrine CCL3 and CCL4 signaling by macrophages and classical monocytes to *CCR5*- and *CCR1*-expressing cDC2 and ThExh (Fig. 4a). Furthermore, classical monocyte derived CXCL10 was predicted to signal to cDC1, ThExh, and Tfh via CXCR3. Nominated inhibitory interactions from ThExh included TIGIT signaling via NECTIN2 expressed by cDC2, classical monocytes, and macrophages (Fig. 4a).

Despite the proximity of cDC2, macrophages, and monocytes to HRSC, the anti-tumor immune response remains inadequate in cHL. The failure of cDC2 to prime an effective T cell response may result from aberrant upregulation of inhibitory ligand and receptor molecules, amplifying immunosuppressive signaling in the HRSC microenvironment. To test this hypothesis, we designed a second IF panel to

examine the expression of PD-L1, IDO1, and TIM-3 on CD11c<sup>+</sup> and CD68<sup>+</sup> cells, and their spatial relationships to CD30<sup>+</sup> HRSC (Table 1). HRSC exhibited extensive PD-L1 expression as expected. In addition, we found an enrichment of PD-L1<sup>+</sup> CD11c<sup>+</sup>/CD68<sup>+</sup> and CD11c<sup>+</sup>/CD68<sup>-</sup> MNPs in CD30<sup>+</sup> HRSC-centric neighborhoods (Fig. 4b-c). Similarly, we found variable coexpression of the co-inhibitory receptor TIM-3, and IDO1 - an immunomodulating tryptophan catabolizing enzyme - on CD11c<sup>+</sup>/CD68<sup>+</sup> and CD11c<sup>+</sup>/CD68<sup>-</sup> MNPs in close proximity to HRSC (Fig. 4c-d, Fig. 5a-d). The proportion of CD11c<sup>+</sup>/CD68<sup>-</sup> and CD11c<sup>+</sup>/CD68<sup>+</sup> MNPs expressing inhibitory molecules increased with age at diagnosis ( $p < 0.05$ ) (Fig. 6a), suggesting immunosuppressive signaling in pediatric and young-adult cHL may differ compared with cHL in older adults. We noted no significant differences in the proportion of MNPs expressing inhibitory molecules according to sex, tumor type, or EBV status (data not shown).

## Discussion

HRSC have the remarkable ability to cohere a tumor mass, mainly composed of potential anti-tumor cells, by establishing an immunosuppressive microenvironment. Therapeutic efforts to reverse this immune suppression have targeted T cells, and specifically the exhaustion marker PD-1, while recent studies provide a rationale for also targeting other immune checkpoints<sup>11,39</sup>. Unbiased scRNAseq profiling of cHL tumors has demonstrated enrichment of exhausted LAG3<sup>+</sup> CD4<sup>+</sup> T-cells around MHCII<sup>-</sup> HRSC<sup>11</sup>, and elaboration of CXCL13 by Tfh-like cells in the TME of lymphocyte-rich cHL<sup>31</sup>. There is a surfeit of immunosuppressive mechanisms in cHL, which may be co-opted dynamically by HRSC.

The mononuclear phagocyte system provides a diverse repertoire of pro-tumor and tumoricidal potential, this plasticity contingent upon the tumor context and paracrine signaling. The MNPs identified in this study are a conspicuous histomorphological feature of cHL, and while pDC and LAMP3<sup>+</sup> aDC are excluded from the HRSC neighborhood, MNPs expressing CD68 and / or CD11c, as well as CD11<sup>+</sup> CD1c<sup>+</sup> cDC2, cluster together and around HRSCs. This inflammatory response should remove apoptotic cells, directly engulf tumor cells, and present cancer-identifying neoantigens to T cells, yet these mechanisms are inhibited. Our findings reveal a network of immunosuppressive MNPs closely associated with PD-L1<sup>+</sup> HRSCs. These MNPs cooperate with HRSC-derived and NF- $\kappa$ B-directed chemokine expression, providing chemoattractant and inhibitory signals that recruit and instruct immunosuppressive T cells. Our analysis identifies classical monocytes in particular as important signaling hubs, controlling retention of cDC2 and ThExh via CCR1-, CCR4-, CCR5-, and CXCR3-dependent signaling (Fig. 4e).

Previous work has highlighted that increased proportions of CD68<sup>+</sup> TAM by immunohistochemistry, and an enhanced macrophage-associated gene expression signature, correlate with inferior clinical outcomes in patients with advanced cHL<sup>40,41</sup>. The positioning of these cells close to HRSC suggests that they have

proximal roles in directing and amplifying the tolerogenic niche. Underlining the importance of the HRSC-associated MNP network, recent reports have demonstrated that eradication of HRSC, following first line anti-PD-1 immune checkpoint blockade, is associated with a reduction in PD-L1<sup>+</sup> TAM, rather than a detectable cytotoxic response<sup>42</sup>..

The substantial co-expression of inhibitory molecules and chemokines by HRSC-associated MNPs indicates functional redundancy in immunosuppressive signaling. This may partially explain resistance to targeting of individual components (e.g. PD-1), and offer opportunities for tailoring therapies on the basis of molecular profiling. In a murine model, it has been shown that TAMs rapidly transfer anti-PD-1 complexes away from T cells, through a FcγR-mediated process<sup>43</sup>. The active recruitment of infiltrating MNPs suggests that plausible strategies for further study could include TAM-depletion, for example by CCL2 inhibition<sup>44,45</sup> or CSF1-CSF1R blockade<sup>46</sup>, although this has proven unsuccessful in solid tumors, perhaps due to rebound infiltration of haematopoietic-origin MNPs after treatment. An alternative is to potentiate monocyte-derived MNPs and macrophages, including by immune checkpoint blockade, CD40 agonism, or CAR-macrophage cell therapy<sup>47</sup>. Theoretically this could simultaneously increase tumor phagocytosis, antigen presentation, and restore effective T-cell priming, thus augmenting both TAM and DC responses.

## Declarations

### Acknowledgements

BJS is supported by a Clinical Doctoral Fellowship from the Wellcome Trust (216366/Z/19/Z).

CDC is supported by grant funding from the JGW Patterson Foundation (<https://jgwpattersonfoundation.co.uk>), Bright Red (<https://brightred.org.uk>), the Lymphoma Research Trust, a Medical Research Council 'Confidence in Concepts' award, and a Wellcome Trust Small project grant award.

We thank Dr Christian Stiedl (The University of British Columbia) for generous sharing of scRNAseq data. We thank the Newcastle University / Newcastle upon Tyne NHS Foundation Trust Molecular diagnostics laboratory (NovoPath; <https://www.novopath.co.uk/>) for tissue handling and technical assistance.

### Author contributions

BJS performed data analysis and wrote the manuscript, MF performed data analysis and contributed to the manuscript, MDY contributed to data curation, CJ, AS, AB, CB, VR, JRF performed scRNAseq

experiments, KTM and KSP acquired deceased donor lymph node tissue, MRC and SB supervised the project, CDC performed microscopy experiments, analysed data, wrote the manuscript, and supervised the project.

### **Conflict of interest**

None declared

### **Code availability**

Code used to analyze data in the project is uploaded to Github at [https://github.com/bjstewart1/hodgkin\\_lymphoma\\_analysis](https://github.com/bjstewart1/hodgkin_lymphoma_analysis)

### **Data availability**

Data is made available to download on this website as an annotated data object (.h5ad file) and interactive cellxgene portal.

## **References**

1. Sasse S, Bröckelmann PJ, Goergen H, et al. Long-Term Follow-Up of Contemporary Treatment in Early-Stage Hodgkin Lymphoma: Updated Analyses of the German Hodgkin Study Group HD7, HD8, HD10, and HD11 Trials. *J. Clin. Oncol.* 2017;35(18):1999–2007.
2. Borchmann P, Goergen H, Kobe C, et al. PET-guided treatment in patients with advanced-stage Hodgkin's lymphoma (HD18): final results of an open-label, international, randomised phase 3 trial by the German Hodgkin Study Group. *Lancet.* 2017;390(10114):2790–2802.
3. Casasnovas R-O, Bouabdallah R, Brice P, et al. PET-adapted treatment for newly diagnosed advanced Hodgkin lymphoma (AHL2011): a randomised, multicentre, non-inferiority, phase 3 study. *Lancet Oncol.* 2019;20(2):202–215.
4. Connors JM, Cozen W, Steidl C, et al. Hodgkin lymphoma. *Nat Rev Dis Primers.* 2020;6(1):61.
5. Roemer MGM, Redd RA, Cader FZ, et al. Major Histocompatibility Complex Class II and Programmed Death Ligand 1 Expression Predict Outcome After Programmed Death 1 Blockade in Classic Hodgkin Lymphoma. *J. Clin. Oncol.* 2018;36(10):942–950.

6. Green MR, Monti S, Rodig SJ, et al. Integrative analysis reveals selective 9p24.1 amplification, increased PD-1 ligand expression, and further induction via JAK2 in nodular sclerosing Hodgkin lymphoma and primary mediastinal large B-cell lymphoma. *Blood*. 2010;116(17):3268–3277.
7. Cader FZ, Hu X, Goh WL, et al. A peripheral immune signature of responsiveness to PD-1 blockade in patients with classical Hodgkin lymphoma. *Nat. Med.* 2020;26(9):1468–1479.
8. Armand P, Engert A, Younes A, et al. Nivolumab for Relapsed/Refractory Classic Hodgkin Lymphoma After Failure of Autologous Hematopoietic Cell Transplantation: Extended Follow-Up of the Multicohort Single-Arm Phase II CheckMate 205 Trial. *J. Clin. Oncol.* 2018;36(14):1428–1439.
9. Ansell SM, Lesokhin AM, Borrello I, et al. PD-1 blockade with nivolumab in relapsed or refractory Hodgkin's lymphoma. *N. Engl. J. Med.* 2015;372(4):311–319.
10. Carey CD, Gusenleitner D, Lipschitz M, et al. Topological analysis reveals a PD-L1-associated microenvironmental niche for Reed-Sternberg cells in Hodgkin lymphoma. *Blood*. 2017;130(22):2420–2430.
11. Aoki T, Chong LC, Takata K, et al. Single-Cell Transcriptome Analysis Reveals Disease-Defining T-cell Subsets in the Tumor Microenvironment of Classic Hodgkin Lymphoma. *Cancer Discov.* 2020;10(3):406–421.
12. Lopez R, Regier J, Cole MB, Jordan MI, Yosef N. Deep generative modeling for single-cell transcriptomics. *Nat. Methods*. 2018;15(12):1053–1058.
13. James KR, Gomes T, Elmentaite R, et al. Distinct microbial and immune niches of the human colon. *Nat. Immunol.* 2020;21(3):343–353.
14. Melsted P, Ntranos V, Pachter L. The barcode, UMI, set format and BUStools. *Bioinformatics*. 2019;35(21):4472–4473.
15. Lun ATL, Riesenfeld S, Andrews T, et al. EmptyDrops: distinguishing cells from empty droplets in droplet-based single-cell RNA sequencing data. *Genome Biol.* 2019;20(1):63.
16. Young MD, Mitchell TJ, Vieira Braga FA, et al. Single-cell transcriptomes from human kidneys reveal the cellular identity of renal tumors. *Science*. 2018;361(6402):594–599.
17. Domínguez CC, Gomes T, Jarvis LB, et al. Cross-tissue immune cell analysis reveals tissue-specific adaptations and clonal architecture across the human body.
18. King HW, Orban N, Riches JC, et al. Single-cell analysis of human B cell maturation predicts how antibody class switching shapes selection dynamics. *Science Immunology*. 2021;6(56):eabe6291.

19. Garreta R, Moncecchi G. Learning scikit-learn: Machine Learning in Python. Packt Publishing Ltd; 2013.
20. Dann E, Henderson NC, Teichmann SA, Morgan MD, Marioni JC. Differential abundance testing on single-cell data using k-nearest neighbor graphs. *Nat. Biotechnol.* 2021;
21. Efremova M, Vento-Tormo M, Teichmann SA, Vento-Tormo R. CellPhoneDB: inferring cell-cell communication from combined expression of multi-subunit ligand-receptor complexes. *Nat. Protoc.* 2020;15(4):1484–1506.
22. Davis S, Meltzer PS. GEOquery: a bridge between the Gene Expression Omnibus (GEO) and BioConductor. *Bioinformatics.* 2007;23(14):1846–1847.
23. Ritchie ME, Phipson B, Wu D, et al. limma powers differential expression analyses for RNA-sequencing and microarray studies. *Nucleic Acids Res.* 2015;43(7):e47.
24. Garcia-Alonso L, Holland CH, Ibrahim MM, Turei D, Saez-Rodriguez J. Benchmark and integration of resources for the estimation of human transcription factor activities. *Genome Res.* 2019;29(8):1363–1375.
25. Türei D, Korcsmáros T, Saez-Rodriguez J. OmniPath: guidelines and gateway for literature-curated signaling pathway resources. *Nat. Methods.* 2016;13(12):966–967.
26. Levine JH, Simonds EF, Bendall SC, et al. Data-Driven Phenotypic Dissection of AML Reveals Progenitor-like Cells that Correlate with Prognosis. *Cell.* 2015;162(1):184–197.
27. Traag VA, Waltman L, van Eck NJ. From Louvain to Leiden: guaranteeing well-connected communities. *Sci. Rep.* 2019;9(1):5233.
28. Love MI, Huber W, Anders S. Moderated estimation of fold change and dispersion for RNA-seq data with DESeq2. *Genome Biol.* 2014;15(12):550.
29. Feng Z, Puri S, Moudgil T, et al. Multispectral imaging of formalin-fixed tissue predicts ability to generate tumor-infiltrating lymphocytes from melanoma. *J Immunother Cancer.* 2015;3:47.
30. Tóth ZE, Mezey E. Simultaneous visualization of multiple antigens with tyramide signal amplification using antibodies from the same species. *J. Histochem. Cytochem.* 2007;55(6):545–554.
31. Aoki T, Chong LC, Takata K, et al. Single-cell profiling reveals the importance of CXCL13/CXCR5 axis biology in lymphocyte-rich classic Hodgkin lymphoma. *Proc. Natl. Acad. Sci. U. S. A.* 2021;118(41.):
32. Villani A-C, Satija R, Reynolds G, et al. Single-cell RNA-seq reveals new types of human blood dendritic cells, monocytes, and progenitors. *Science.* 2017;356(6335.):

33. Park J-E, Botting RA, Domínguez Conde C, et al. A cell atlas of human thymic development defines T cell repertoire formation. *Science*. 2020;367(6480.):
34. Madisson E, Wilbrey-Clark A, Miragaia RJ, et al. scRNA-seq assessment of the human lung, spleen, and esophagus tissue stability after cold preservation. *Genome Biol*. 2019;21(1):1.
35. Maier B, Leader AM, Chen ST, et al. A conserved dendritic-cell regulatory program limits antitumour immunity. *Nature*. 2020;580(7802):257–262.
36. Steidl C, Diepstra A, Lee T, et al. Gene expression profiling of microdissected Hodgkin Reed-Sternberg cells correlates with treatment outcome in classical Hodgkin lymphoma. *Blood*. 2012;120(17):3530–3540.
37. Nagel D, Vincendeau M, Eitelhuber AC, Krappmann D. Mechanisms and consequences of constitutive NF- $\kappa$ B activation in B-cell lymphoid malignancies. *Oncogene*. 2014;33(50):5655–5665.
38. International Agency for Research on Cancer, World Health Organization. WHO Classification of Tumours of Haematopoietic and Lymphoid Tissues. World Health Organization; 2008.
39. Patel SS, Weirather JL, Lipschitz M, et al. The microenvironmental niche in classic Hodgkin lymphoma is enriched for CTLA-4-positive T cells that are PD-1-negative. *Blood*. 2019;134(23):2059–2069.
40. Steidl C, Lee T, Shah SP, et al. Tumor-associated macrophages and survival in classic Hodgkin's lymphoma. *N. Engl. J. Med*. 2010;362(10):875–885.
41. Tan KL, Scott DW, Hong F, et al. Tumor-associated macrophages predict inferior outcomes in classic Hodgkin lymphoma: a correlative study from the E2496 Intergroup trial. *Blood*. 2012;120(16):3280–3287.
42. Reinke S, Bröckelmann PJ, Iaccarino I, et al. Tumor and microenvironment response but no cytotoxic T-cell activation in classic Hodgkin lymphoma treated with anti-PD1. *Blood*. 2020;136(25):2851–2863.
43. Arlauckas SP, Garris CS, Kohler RH, et al. In vivo imaging reveals a tumor-associated macrophage-mediated resistance pathway in anti-PD-1 therapy. *Sci. Transl. Med*. 2017;9(389.):
44. Cassetta L, Pollard JW. Targeting macrophages: therapeutic approaches in cancer. *Nat. Rev. Drug Discov*. 2018;17(12):887–904.
45. Teng K-Y, Han J, Zhang X, et al. Blocking the CCL2-CCR2 axis using CCL2-neutralizing antibody is an effective therapy for hepatocellular cancer in a mouse model. *Mol. Cancer Ther*. 2017;16(2):312–322.
46. Pyonteck SM, Akkari L, Schuhmacher AJ, et al. CSF-1R inhibition alters macrophage polarization and blocks glioma progression. *Nat. Med*. 2013;19(10):1264–1272.

47. Klichinsky M, Ruella M, Shestova O, et al. Human chimeric antigen receptor macrophages for cancer immunotherapy. *Nat. Biotechnol.* 2020;38(8):947–953.

## Tables

Table 1. Clinical and Pathological Characteristics of Classic Hodgkin Lymphoma Study Cases for Multiplexed Immunofluorescence and Nanostring

Study Tumor Reference	Disease Subtype	EBV Status	GeoMx	Age at Diagnosis (years)	Sex	Site of Biopsy (Excised Node)	Stage	Clinical Response
CHL-1	MCCHL	NEG		80	M	Inguinal	2A	CR
CHL-3	MCCHL	NEG		77	F	Submandibular	NA	CR / relapse
CHL-4	LRCHL	POS		75	F	Neck	2A	CR
CHL-5	NSCHL	NEG		73	F	Supraclavicular	4B	CR
CHL-6	NSCHL	NEG		73	M	Neck	1A	CR
CHL-7	NSCHL	NEG		72	M	Neck	1A	CR
CHL-9	NSCHL	NEG	YES	69	M	Neck	1A	PD / Salvage CR
CHL-10	NSCHL	NEG	YES	69	F	Neck	3B	CR
CHL-11	CHL-NOS	POS		68	F	Neck	3B	CR / relapse
CHL-12	CHL-NOS	POS		68	F	Axilla	1A	CR / relapse
CHL-13	MCCHL	NEG		68	M	Inguinal	2A	CR
CHL-14	CHL-NOS	NEG		64	M	Mediastinum	NA	PD / salvage CR
CHL-15	MCCHL	POS		64	M	Neck	NA	NA
CHL-16	MCCHL	NEG		63	F	Neck	2A	CR
CHL-18	MCCHL	POS		60	F	Supraclavicular	4B	CR
CHL-19	MCCHL	NA		53	M	Inguinal	NA	PD
CHL-20	LRCHL	NA		46	M	Axilla	NA	NA
CHL-21	MCCHL	POS		45	M	Neck	3S	PD
CHL-22	NSCHL	POS		40	M	Neck	2A	CR / relapse
CHL-23	NSCHL	POS		39	M	Neck	4A	PR / salvage CR
CHL-24	NSCHL	NA		38	M	Supraclavicular	4A	PD
CHL-25	NSCHL	NEG		33	F	Neck	3B	CR
CHL-27	NSCHL	POS	YES	32	M	Supraclavicular	2A	PD
CHL-28	MCCHL	POS		32	M	Neck	3B	CR
CHL-29	NSCHL	NA		32	M	Neck	4A	CR / relapse
CHL-30	MCCHL	POS		28	F	Neck	2A	CR
<b>Study</b>	<b>Disease</b>	<b>EBV</b>	<b>GeoMx</b>	<b>Age at</b>	<b>Sex</b>	<b>Site of Biopsy</b>	<b>Stage</b>	<b>Clinical</b>

Tumor	Subtype	Status		Diagnosis (years)		(Excised Node)		Response
CHL-31	NSCHL	NEG		28	M	Neck	4B	CR
CHL-32	MCCHL	POS	YES	26	M	Neck	2A	CR
CHL-33	NSCHL	POS		25	M	Neck	2B	CR
CHL-34	NSCHL	NEG	YES	24	M	Neck	NA	NA
CHL-36	NSCHL	NEG		23	F	Neck	2A	CR
CHL-39	MCCHL	NEG		22	F	Supraclavicular	NA	NA
CHL-40	NSCHL	NEG	YES	20	M	Supraclavicular	3BS	CR
CHL-41	NSCHL	NEG		19	F	Mediastinum	2B	PD / salvage
CHL-42	NSCHL	NEG		18	F	Neck	2B	PD
CHL-43	NSCHL	NEG	YES	18	M	Neck	2A	CR
CHL-44	NSCHL	POS		18	M	Post nasal space	1A	CR
CHL-45	NSCHL	NEG		17	M	Neck	2A	CR / relapsed & salvage
CHL-48	NSCHL	NEG		16	F	Axilla	3A	PD / salvage
CHL-49	MCCHL	POS		16	M	Axilla	1A	CR / relapsed & salvage
CHL-50	NSCHL	NEG		16	F	Neck	2A	CR
CHL-51	NSCHL	POS		16	F	Supraclavicular	3B	CR
CHL-52	NSCHL	NA		15	F	Neck	2B	CR
CHL-53	CHL-NOS	NEG		14	F	Retroperitoneal	3B	CR
CHL-54	NSCHL	NEG	YES	14	M	Supraclavicular	2A	CR
CHL-55	CHL-NOS	NEG		14	F	Supraclavicular	3A	CR
CHL-56	NSCHL	NEG		14	F	Neck	4A	CR
CHL-57	NSCHL	NEG	YES	14	M	Supraclavicular	2A	CR
CHL-59	NSCHL	NEG	YES	13	M	Neck	4A	CR
CHL-60	LR-CHL	POS		12	M	Neck	1A	CR
CHL-61	NSCHL	POS		12	M	Neck	2B	CR
CHL-62	MCCHL	POS		8	M	Hilar	4A	CR / relapsed &

								salvage
<b>CHL-63</b>	CHL-NOS	POS		7	M	Neck	4B	CR
<b>Study Tumor</b>	<b>Disease Subtype</b>	<b>EBV Status</b>	<b>GeoMx</b>	<b>Age at Diagnosis (years)</b>	<b>Sex</b>	<b>Site of Biopsy (Excised Node)</b>	<b>Stage</b>	<b>Clinical Response</b>
<b>CHL-64</b>	MCCHL	POS		6	F	Neck	3B	CR

NA = Not available

**Disease Subtypes (n=54)**

- NSCHL = Nodular Sclerosis Classical Hodgkin Lymphoma (n=30 / 55.6%)
- MCCHL = Mixed Cell Classical Hodgkin Lymphoma (n=15 / 27.8%)
- LRCHL = Lymphocyte rich Classical Hodgkin Lymphoma (n=3 / 5.6%)
- CHL-NOS = Classical Hodgkin Lymphoma, Not otherwise specified (n=6 / 11.1%)

**EBV Status**

- Epstein-Barr virus, as assessed by Epstein-Barr virus (EBV)-encoded small RNAs (EBERs).

**GeoMx**

- Tumor biopsies selected for Nanostring GeoMx assay.

**Stage**

- Ann Arbor staging classification of lymphoma

**Clinical Response**

- Best response with first-line treatment / any further event and treatment
- CR = complete remission or complete metabolic response
- PD = progressive disease

Table 2 - Antibodies and secondary reagents used for multiplex immunofluorescence panels

	Primary Antibody	Primary Antibody Dilution	Clone	Manufacturer	Secondary Antibody (Ventana)	TSA-Conjugated Fluorochrome
1	CD11c	1:200	5D11	Leica	Omnimap	Opal-520
2	CD30	1:25	BerH2	Cell Marque	Ultramap	Opal-540
3	CD68P <sup>□</sup>	1:1500	PGM1	Dako	Omnimap	Opal-570
4	IDO1 <sup>□</sup>	1:4000	V1NC3IDO	Invitrogen	Omnimap	Opal-620
5	PD-L1 <sup>□</sup>	Pre-dilute	SP263	Ventana	Optiview	Opal-650
6	TIM-3 <sup>□</sup>	1:200	D5D5R	Cell Signaling Technology	Omnimap	Opal-690
7	CADM1*	1:10,000	Polyclonal	Sigma-Aldrich	Omnimap	Opal-570
8	CD1C*	1:100	OTI2F4	Abcam	Omnimap	Opal-620
9	LAMP3*	1:100	1010E1	Dendritics	Ultramap	Opal-650
10	CD123*	1:200	BR4MS	Leica	Optiview	Opal-690

TSA = Tyramide signal amplification.

CD11c & CD30 are used in both multiplexes. Other antibodies are annotated, as below:

□ Multiplex 1 only

\* Multiplex 2 only

## Figures

Figure 1

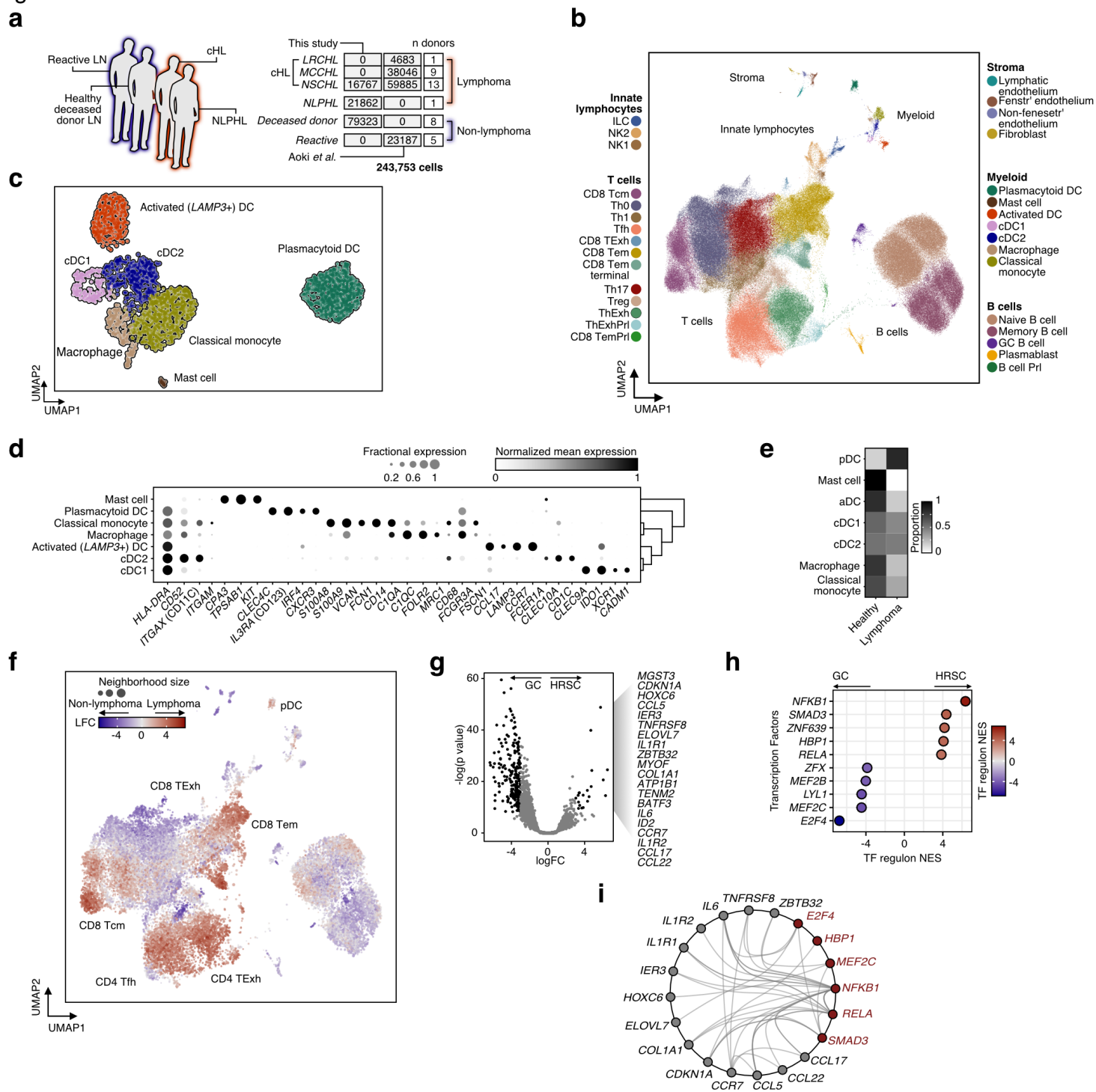


Figure 1

Transcriptional profiling of cell types in the cHL microenvironment. a. Outline of the

scRNAseq dataset. Two datasets (Aoki et al. and “this study”/WSI dataset) were merged, and contain data from lymph nodes unaffected by lymphoma (reactive lymph nodes and healthy lymph nodes from

deceased donors) highlighted in blue, and lymphoma-infiltrated lymph nodes highlighted in red. The numbers of cells are given in dark gray, and the number of donors in light gray. b. UMAP plot of 243,753 cells from an integrated scRNAseq dataset colored by cell type and organized by compartment (T cells, B cells, innate lymphocytes, myeloid, and stroma). c. UMAP plot of 2727 myeloid cells colored by cell type. d. Heatmap showing mean normalized expression levels (color) and fraction of cells expressing (dot size) markers of myeloid cell subsets. e. Heatmap showing the proportion of each cell type derived from healthy and lymphoma samples. f. UMAP plot of 22,573 graph neighborhoods, colored by the differential abundance (log fold change) in lymphoma affected or non lymphoma affected (deceased-donor lymph nodes or reactive lymph node) samples. Dot size is proportional to neighborhood size (median neighborhood size = 50 cells). g. Volcano plot showing differentially expressed genes between microdissected GC and HRSC. Significant genes for HRSC are indicated ( $|\text{LFC}| > 3$ , adjusted p value  $< 0.01$ ). h. Heatmap showing transcription factor (TF) regulon normalized enrichment scores for GC vs HRSC calculated with DoRothEA. i. Graph indicating predicted interactions between genes (red, transcription factors; gray, other genes) differentially expressed in HRSC. Edges drawn where an interaction is documented by OmniPath.

Figure 2

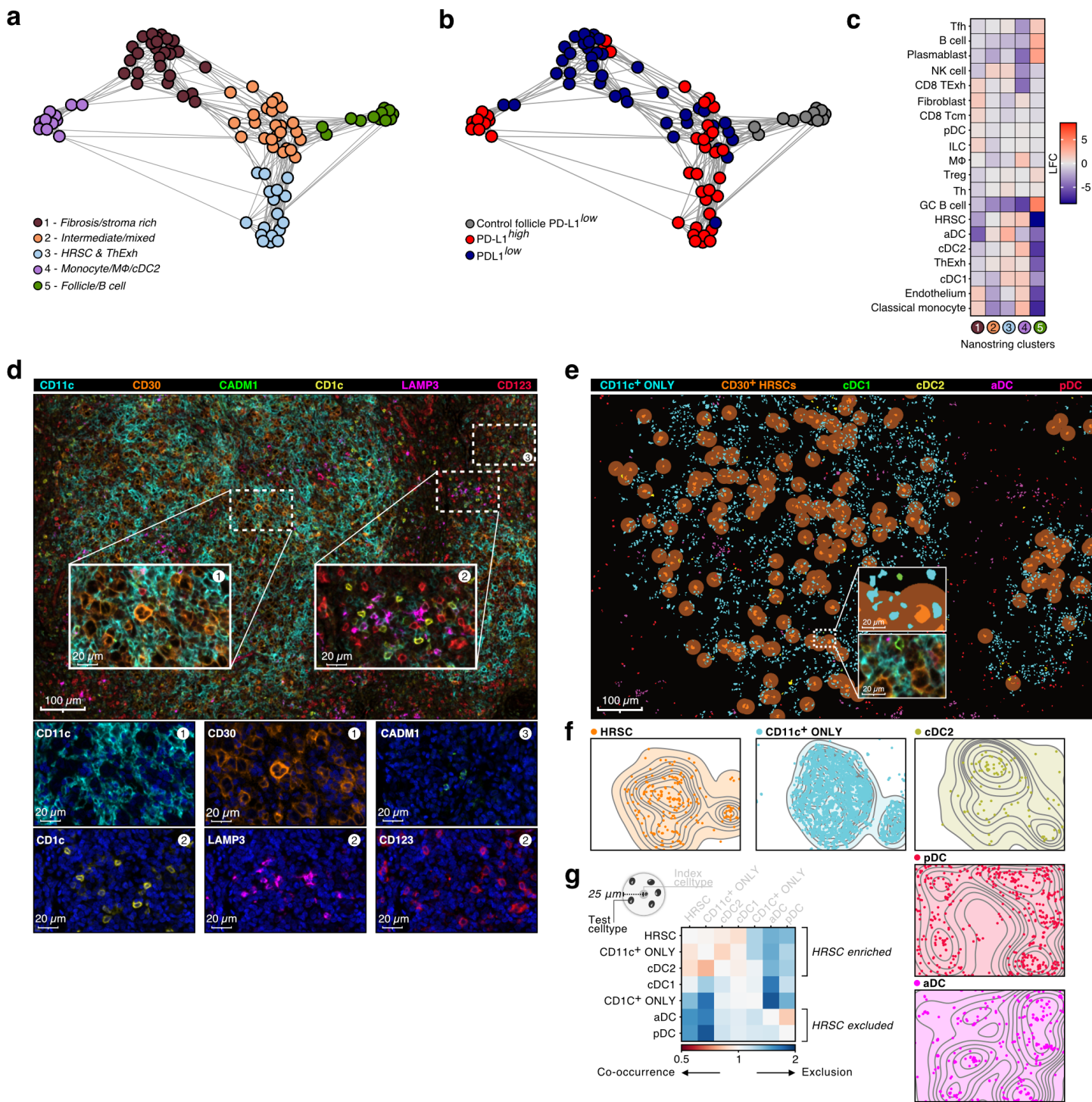


Figure 2

**Mononuclear phagocyte enrichments in the Hodgkin Reed-Sternberg cell microenvironment.** **a.** Shared nearest-neighbor graph embedding of transcriptional profiles of nanostring ROI from reactive and cHL lymph nodes. Color indicates clusters identified using Leiden clustering with resolution = 1. **b.** Shared nearest-neighbor graph embedding of transcriptional profiles of nanostring ROI colored by PD-L1 expression status. **c.** Differential abundance estimates of cell-types deconvolved from nanostring ROI

between clusters shown in (a), LFC estimates represent differential abundance of cell-types in each cluster vs all other clusters. **d.** Representative micrographs from multiplexed IF imaging of cHL samples. One of 3 test regions from tumor CHL-27 is shown, cropped to 1662  $\mu\text{m}$  by 1076  $\mu\text{m}$ ; CD11c (cyan), CD30 (orange), CADM1 (green), CD1c (yellow), LAMP3 (magenta), and CD123 (red) fluorescent signals are represented by unique pseudocolors. To improve clarity DAPI is not shown. Selected areas are highlighted, each at 100x magnification (160  $\mu\text{m}$  x 108  $\mu\text{m}$ ); CD30+ HRSC-dense area (region 1, inset left), internodular area with no CD30+ HRSC (region 2, inset right), and area with CADM1+ cDC1 (region 3, inset top right). Individual pseudocolors are shown below the main image (second & third lines), with DAPI (blue) to identify cell nuclei. Each individual image refers to a multiplexed area above (inset), indicated by the corresponding number (top right). **e.** HRSC and DC map, corresponding to the same region from (d). Phenotyped cells are identified by colored nuclei, with each cell type represented by a different color; 'CD11c+ ONLY' (CD11c+ CD1c-, cyan), CD30+ HRSC (light orange), cDC1 (green), cDC2 (yellow), LAMP3+ aDC (magenta), and pDC (red) are shown. Cells with no assigned phenotype ('null') and 'CD1c+ ONLY' cells are excluded from this visualization. The 'HRSC neighborhood' is shown as circles surrounding each CD30+ HRSC (dark orange). A selected area is highlighted, at 200x magnification (80  $\mu\text{m}$  x 54 $\mu\text{m}$ ; inset, center); **f.** Isobar plots show the location and density of each cell phenotype of interest, for the corresponding tumor region from (d) and (e) (note the uncropped 2008  $\mu\text{m}$  by 1502  $\mu\text{m}$  region is shown here). HRSCs (orange dots, left) and DC subsets (colors corresponding to each phenotype, right) are shown. **g.** Summarized interaction plot across all study tumors in aggregate, displaying the ratio of the nearest neighbor distance between phenotype pairs (index cell type (gray) to test cell type (black)) compared to the expected baseline distance. Red indicates cell type co-occurrence, blue indicates cell type exclusion.

Figure 3

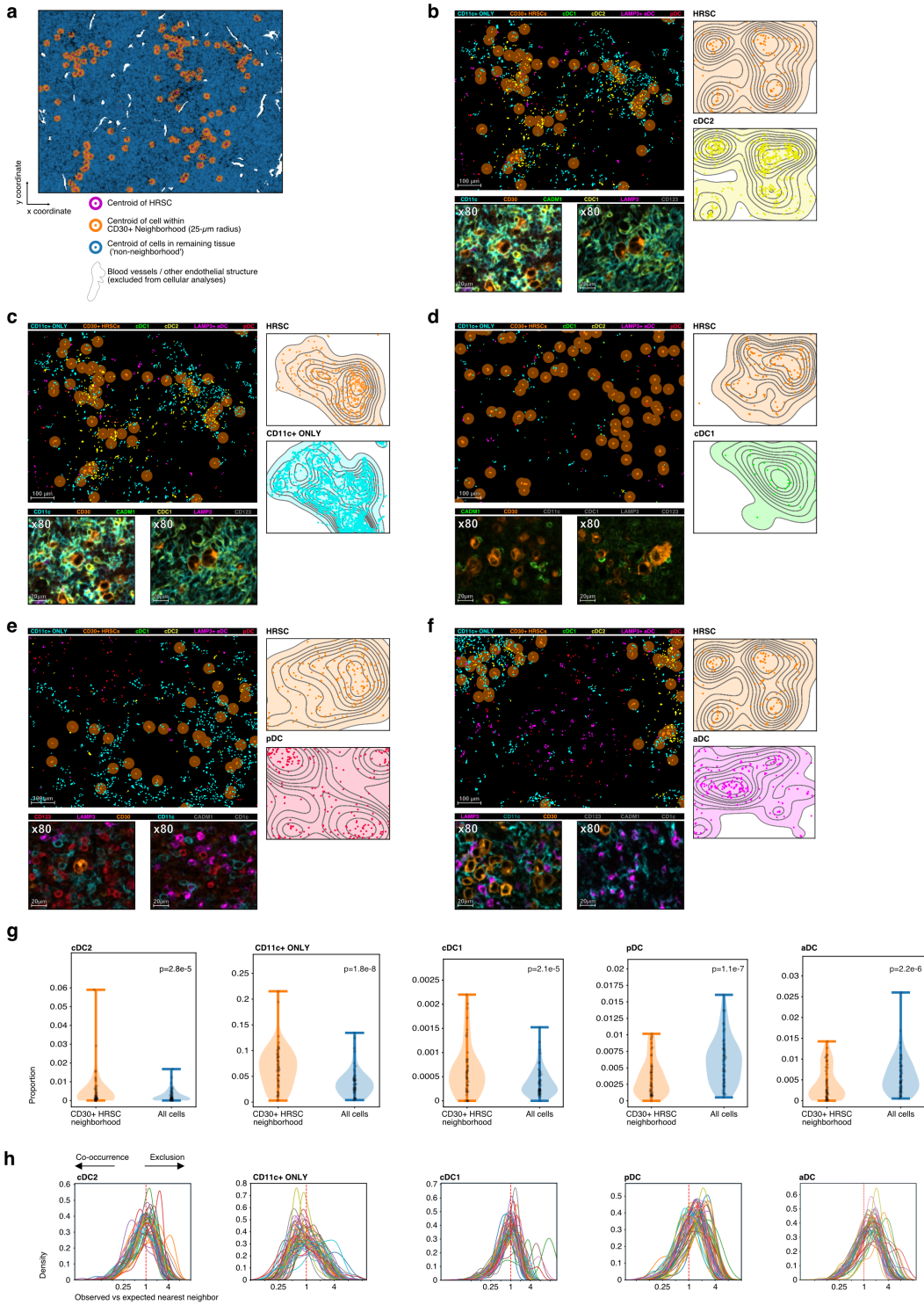


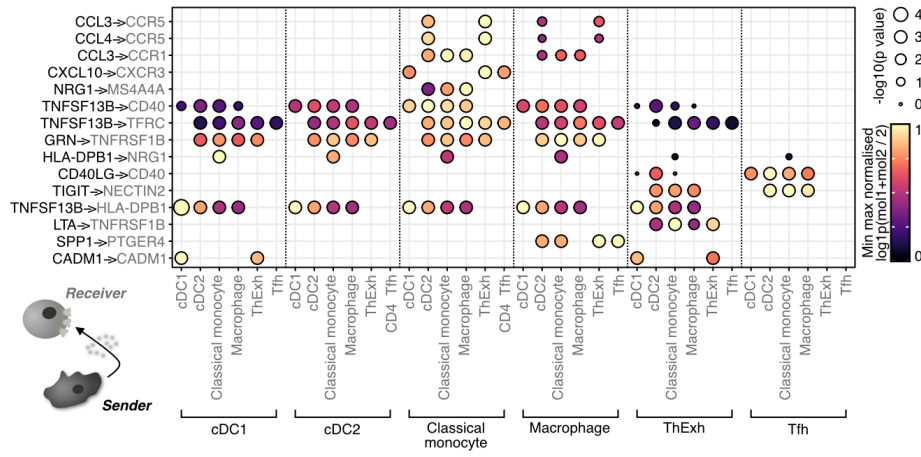
Figure 3

Multiplexed immunofluorescence identifies mononuclear phagocyte enrichment patterns in the Hodgkin Reed-Sternberg cell microenvironment. a. Representative region from CHL-13, which measures 2008  $\mu$ m (x-axis) by 1502  $\mu$ m (y-axis). The centroid of each cell is identified with a colored circle. The CD30+ HRSC are indicated by a magenta circle. The cell nuclei which lie within a 10-25- $\mu$ m radius from each HRSC centroid ('HRSC neighborhood') are indicated by orange circles and those nuclei beyond the 25- $\mu$ m areas

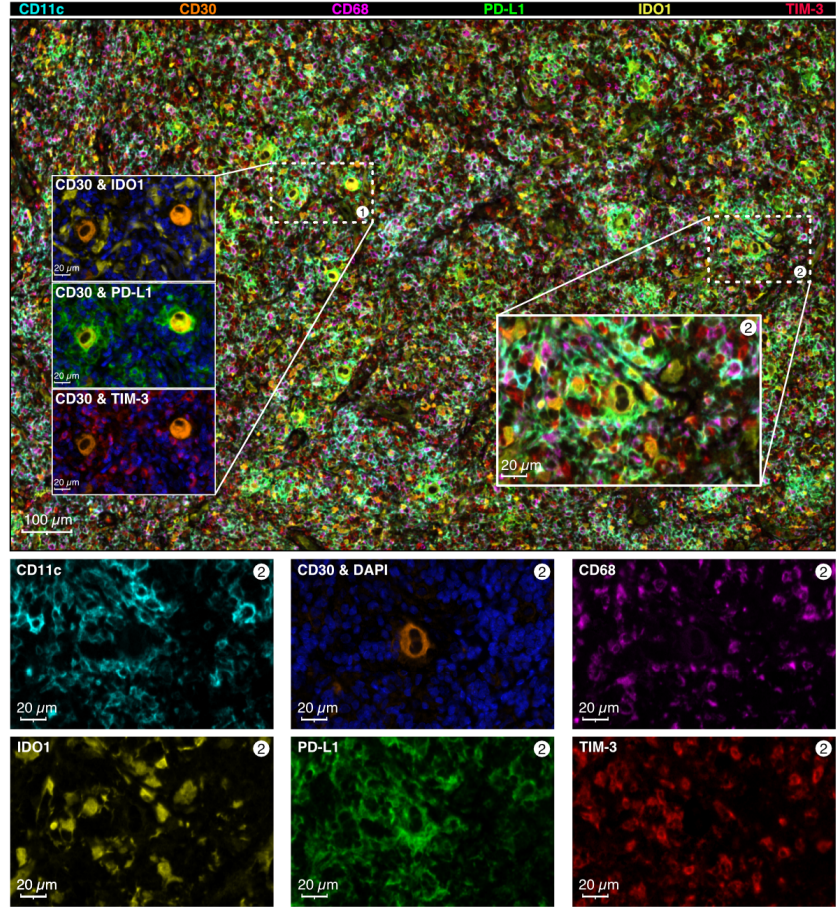
(‘non-neighborhood’) are indicated by blue circles. Blood vessels / other endothelial structures are indicated (white) and all cells encompassed within these areas are excluded from analysis. b, c, d. Spatial distribution of dendritic cell subtypes that co-occur with HRSC. For each phenotype a representative tumor region is identified and shown in all plots: b. cDC2 (CD11c+ CD1c+) = represented by CHL-13. c. CD11c+ ONLY cells = CHL-43. d. cDC1 = CHL-31. e, f. Spatial distribution of dendritic cell subtypes that are ‘excluded’ from HRSC. For each phenotype a representative tumor region is identified and shown in all plots: e. pDC = CHL11. f. aDC / LAMP3+ = CHL-13. A cropped, illustrative area from each tumor region (measuring 1004  $\mu\text{m}$  by 751  $\mu\text{m}$ , left) is shown as a cell map; phenotyped cells are identified by colored nuclei, with each cell type represented by a different color. ‘CD11c+ ONLY’ (cyan), CD30+ HRSC (light orange), cDC1 (green), cDC2 (yellow), LAMP3+ aDC (magenta), and pDC (red) are shown. Cells with no assigned phenotype (‘null’) and ‘CD1c+ ONLY’ cells are excluded from this visualization. The ‘HRSC neighborhood’ is shown as circles surrounding each CD30+ HRSC (dark orange), each circle extending to a radius of 25  $\mu\text{m}$  around each HRSC. Topological maps of the corresponding full region of interest (2008  $\mu\text{m}$  by 1502  $\mu\text{m}$ ) of HRSC (orange, upper right), immune cells of interest (colored according to cell phenotype, lower right). Representative immunofluorescence images (80x magnification), showing cells of interest (second line). CD11c (cyan), CD30 (orange), CADM1 (green), CD1c (yellow), LAMP3 (magenta), and CD123 (red) fluorescent signals are represented by unique pseudocolors. To improve visualization, certain signals may not be shown in each particular image (these excluded colors are shown in gray in each respective key). g. Violin plots comparing the observed cell proportions for each tumor sample for the CD30+ HRSC Neighborhood (orange) and across the entire examined tissue area (‘all cells’; blue), for each DC subtype. Statistical significance: QQ plots showed that the differences in cell proportions between the CD30 neighborhood and the entire sample were not normally distributed, so a Wilcoxon signed-rank test was used to assess statistical significance for each phenotype. h. Histograms showing the distance from each HRSC to its nearest-neighbor of an immune-phenotype. Distance is shown as a ratio to the expected distance if the immune cell were distributed randomly within the tissue section, with values less than 1 (left of dotted line) indicating that cells co-occur with HRSC and values greater than 1 (right of dotted line) indicating that cells are excluded from HRSC.

Figure 4

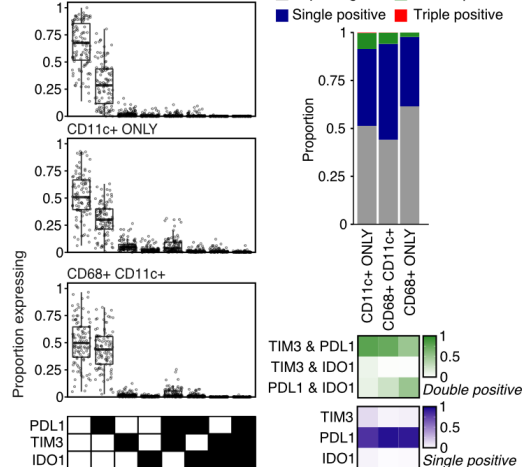
a



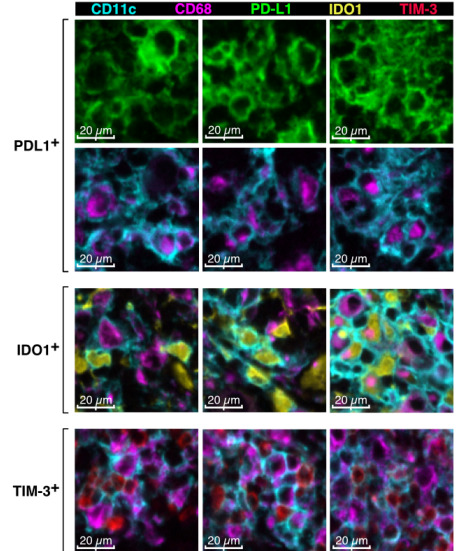
b



c



d



e

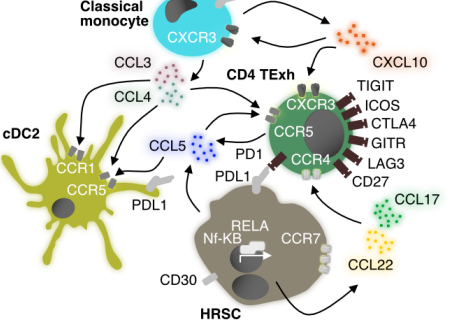


Figure 4

Reciprocal mononuclear phagocyte chemokine and immune checkpoint signalling shapes the immunosuppressive microenvironment in cHL. a. Heatmap of reciprocal ligand-receptor interactions between myeloid subsets and T cells implicated in the cHL TME. Point size indicates permutation p value (CellPhoneDB). Color indicates the min-max normalised aggregate mean expression level of ligand and receptor. b. Representative micrographs from multiplexed IF imaging of cHL samples, showing

expression of inhibitory molecules (IDO1, PD-L1, & TIM-3), celltype defining markers for MNPs (CD11c & CD68), and HRSC (CD30). One of 3 test regions from CHL-7 is shown (2008  $\mu\text{m}$  x 1502  $\mu\text{m}$ ), with CD11c (cyan), CD30 (orange), CD68 (magenta), PD-L1 (green), IDO1 (yellow), and TIM-3 (red) fluorescent signal represented by unique pseudocolors (to improve clarity DAPI is not shown). Inset 1 (100x magnification [160  $\mu\text{m}$  x 108  $\mu\text{m}$ ]; left) shows CD30 and IDO1 (top), CD30 and PD-L1 (middle), and CD30 and TIM-3 (bottom), with DAPI (blue) to identify cell nuclei. Inset 2 (100x magnification [160  $\mu\text{m}$  x 108  $\mu\text{m}$ ], right) shows representative CD30+ HRSC, surrounded by mononuclear phagocytes in closer detail. Individual pseudocolors from area 2, corresponding to each antibody, are shown below the main image (second & third lines). c. Proportion of mononuclear phagocytes expressing immune checkpoints and IDO1. Left panel: lower key represents the combinations of inhibitory molecules (black, expressed; white, unexpressed) corresponding to the proportions shown in boxplots, individual points correspond to cHL cases. Right upper panel: proportions of each cell type expressing, none, one, two or three inhibitory molecules in aggregate across all images. Right lower panel: Proportion of single or double positive cells expressing each indicated combination of inhibitory molecules. d. Expression of PD-L1, IDO1, and TIM-3 by MNPs. Representative images at 200x magnification (54  $\mu\text{m}$  x 54 $\mu\text{m}$ ) show PD-L1 expression (green, top line) and corresponding CD11c (cyan) and CD68 (magenta, second line) for the same areas. Images are separated to improve clarity, as co-localized. IDO1 expression (yellow, cytoplasmic localization) with CD11c and CD68 (third line). TIM-3 expression (red, cytoplasmic localization) with CD11c and CD68 (bottom line). e. Model for intercellular interactions between MNP, dysfunctional T cells, and HRSC in the cHL TME. HRSC produce CCL22, CCL17, and CCL5 downstream of NF- $\kappa$ B activity, orchestrating T-cell recruitment via indicated ligand receptor interactions. CCL3, CCL4, and CXCL10 produced by monocytes directs positioning of dysfunctional T-cells and cDC2. Widespread inhibitory molecule expression is seen on HRSC, MNP, and T cells.

Figure 5

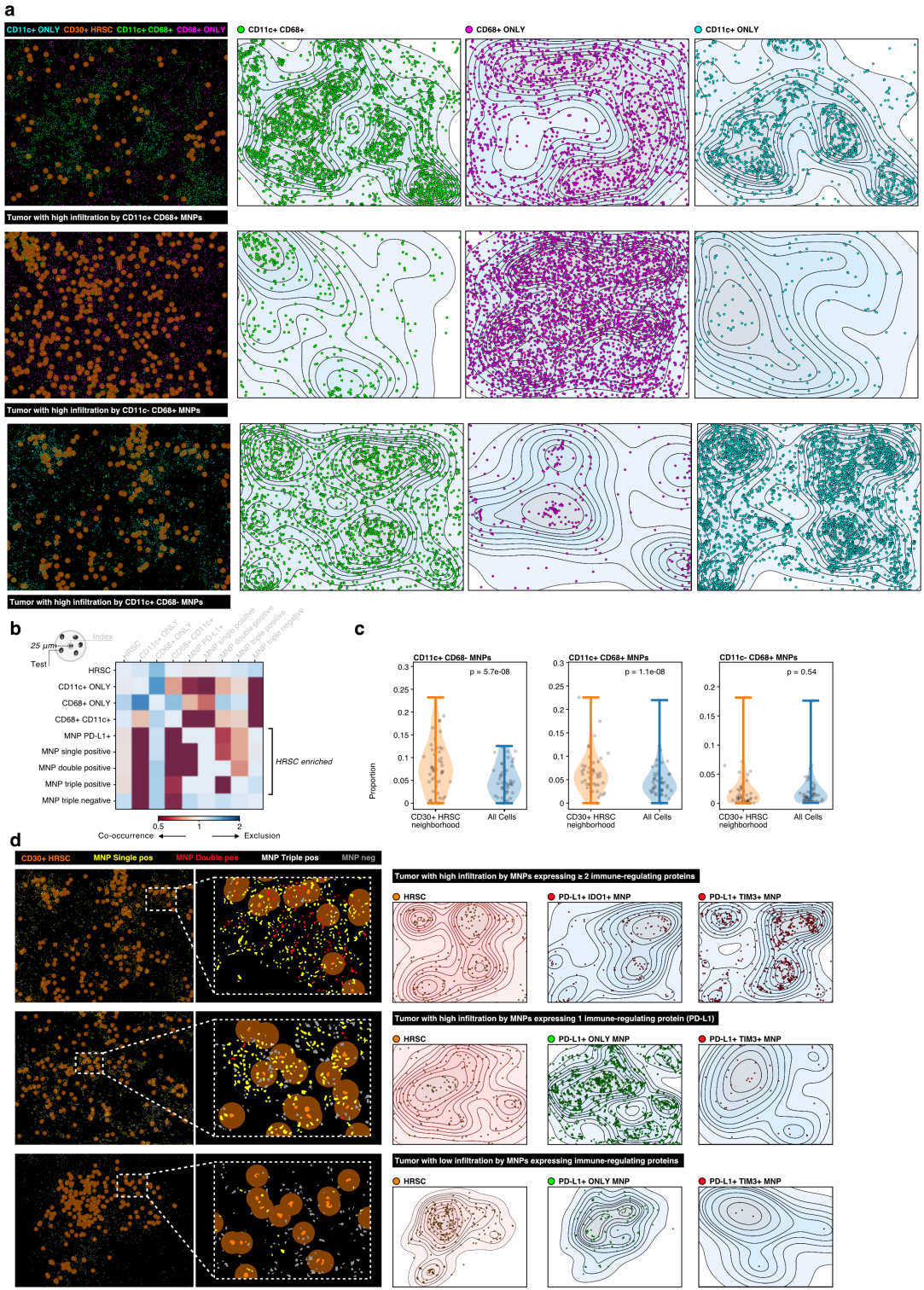


Figure 5

**Mononuclear phagocyte (MNP) infiltration patterns in cHL.** a. Heterogeneity of MNP subtypes across different tumors. Representative 2008  $\mu$ m (x-axis) by 1502  $\mu$ m (y-axis) regions from tumors with high infiltration of: CD11c+ CD68+ MNPs (top panel, tumor 'CHL-12'), CD11c- CD68+ MNPs (middle panel, tumor 'CHL-28'), CD11c+ CD68- MNPs (bottom panel, tumor 'CHL-13'). The nuclei of different cell types are identified by unique colors. CD30+ HRSC are indicated by orange nuclei; the areas surrounding each

HRSC nucleus ('HRSC neighborhood', 25- $\mu\text{m}$  radius from HRSC centroid) are indicated by dark orange rings. The nuclei of CD11c+ CD68+ MNPs (green), CD11cCD68+ MNPs ('CD68+ ONLY', magenta), and CD11c+ CD68- MNPs ('CD11c+ ONLY', cyan) are also shown (left panel). All other cell nuclei are excluded from the visualization. Topological maps of individual MNP subtypes for the corresponding tissue region (2008  $\mu\text{m}$  by 1502  $\mu\text{m}$ ) are shown from left to right, colored according to cell phenotype in the indicated panels. b. Summarized interaction plot across all study tumors in aggregate, displaying the ratio of the nearest neighbor distance between phenotype pairs (index phenotype (gray) to test phenotype (black)) compared to the expected baseline distance. Red indicates cell type co-occurrence, blue indicates cell type exclusion. c. Violin plots comparing the observed cell proportions for each tumor sample for the CD30+ Neighborhood (orange) and across the entire examined tissue area ('all cells'; blue), for each MNP subtype. Wilcoxon signed-rank test used to assess statistical significance.

d. Heterogeneity of the expression of immune-regulating proteins by MNPs surrounding HRSC. 'MNP' encompasses CD11+ CD68-, CD11c+ CD68+, and CD11c- CD68+ cells. The nuclei of different cell types are identified by unique colors. CD30+ HRSC are indicated by orange nuclei; the areas surrounding each HRSC nucleus ('HRSC neighborhood', 25- $\mu\text{m}$  radius from HRSC centroid) are indicated by dark orange rings. MNP that express one of PD-L1, TIM-3, or IDO1 ('MNP single pos') are indicated by yellow nuclei. MNP that express a combination of two of PD-L1, TIM-3, and IDO1 (in any combination) are indicated by red nuclei. MNP that express all PD-L1, TIM-3, and IDO1 are indicated by white nuclei. A range of different expression patterns by the MNP infiltrate are represented.

Top line: representative region from a tumor with high infiltration by MNPs expressing 2 or more immunoregulatory proteins (tumor 'CHL-13'), which measures 2008  $\mu\text{m}$  (x-axis) by 1502  $\mu\text{m}$  (y-axis) (left). A selected area is cropped to provide greater detail (335  $\mu\text{m}$  by 150  $\mu\text{m}$ ; inset). Topological maps of the corresponding tissue region (2008  $\mu\text{m}$  by 1502  $\mu\text{m}$ ) of HRSC (orange dots), PD-L1+ IDO1+ MNP (red dots), and PD-L1+ TIM-3+ MNP (red dots) are shown (right).

Middle line: representative region from a tumor with high infiltration by MNPs expressing 1 or more immunoregulatory protein (tumor 'CHL-51'), which measures 2008  $\mu\text{m}$  (x-axis) by 1502  $\mu\text{m}$  (y-axis) (left). A selected area is cropped to provide greater detail (335  $\mu\text{m}$  by 150  $\mu\text{m}$ ; inset). Topological maps of the corresponding tissue region (2008  $\mu\text{m}$  by 1502  $\mu\text{m}$ ) of HRSC (orange dots), PD-L1+ IDO1- TIM-3- MNP (green dots, 'PD-L1+ only MNP'), and PD-L1+ TIM-3+ MNP (red dots) are shown (right).

Bottom line: representative region from a tumor with high infiltration by MNPs expressing no immunoregulatory proteins (tumor 'CHL-57'), which measures 2008  $\mu\text{m}$  (x-axis) by 1502  $\mu\text{m}$  (y-axis) (left). A

selected area is cropped to provide greater detail (335  $\mu\text{m}$  by 150  $\mu\text{m}$ ; inset). Topological maps of the corresponding tissue region (2008  $\mu\text{m}$  by 1502  $\mu\text{m}$ ) of HRSC (orange dots), PD-L1+ IDO1- TIM-3- MNP (green dots, 'PD-L1+ only MNP'), and PD-L1+ TIM-3+ MNP (red dots) are shown (right).

Figure 6

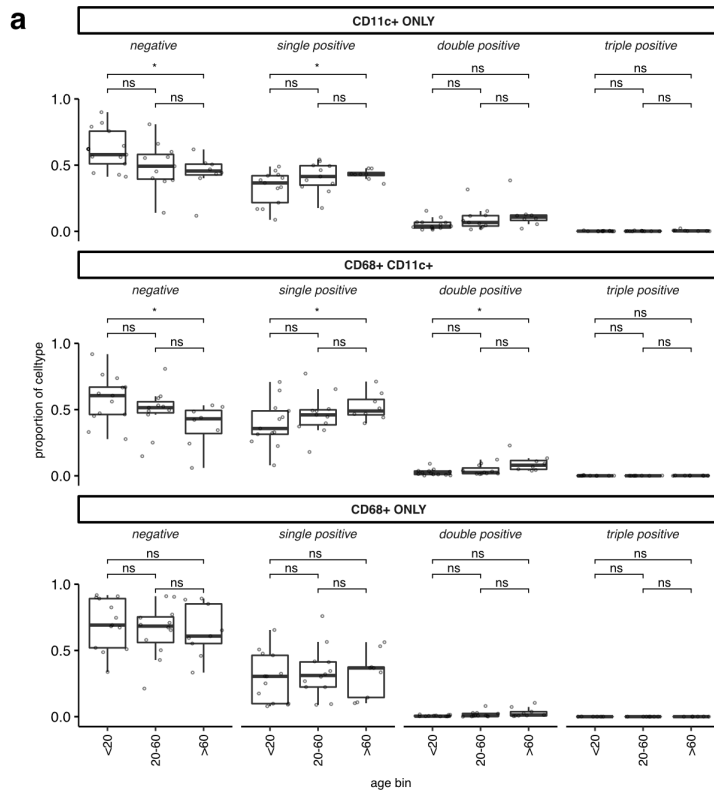


Figure 6

**Mononuclear phagocyte expression of immuno-regulatory molecules increases with age in cHL. a.** Boxplots showing the proportion of each indicated cell category (CD11c + ONLY, CD68 + CD11c+ , and CD68 + ONLY) identified in the multiplexed immunofluorescence panel shown in Fig 3 expressing no (negative), one (single positive), two (double positive), or all three (triple positive) of PD-L1, IDO1, and TIM-3. Statistical significance determined by an unpaired t-test is shown between the indicated contrasts (\*,  $p < 0.05$ ; ns, not significant).

## Supplementary Files

This is a list of supplementary files associated with this preprint. Click to download.

- [SupplementaryBlood03.03.2022.docx](#)

- BldfigS1.tiff
- BldfigS1.tiff
- BldfigS3.tiff